## Part IV : Solid-Solid Phase Transformations I
## Module 1 : Precipitation

# Part IV. Solid-solid transformations I

In this part, we discuss a few of the important solid-solid transformations, namely, precipitation, cellular precipitation, eutectoid transformation, massive transformation, and, martensitic transformation using case studies of certain important engineering and model materials. Our discussion is primarily based on Porter, Easterling and Sherif [1]; we also refer the reader to a concise text book by Raghavan [2] for further reading on some of the aspects that we discuss here.

# 1. Precipitation

## 1.1 Motivation

In carbon steels, quenching leads to hardening while in aluminium alloys (Al-Cu for example) quenching leads to softening. Why?

## 1.2 Al-Cu alloys

Age hardenabale alloys are one of the most important classes of alloys both from the practical and scientific points of view: from a practical viewpoint, they are important because they show that by a suitable heat treatment of solutionising and aging, it is possible to improve mechanical properties; from a scientific viewpoint, in age hardenable alloys, the correlation between microstructure and mechanical properties as well as the methodology of manipulation of the microstructures through appropriate phase transformation is very clearly seen.

### 1.2.1 Solutionising

The aging heat treatment is usually preceded by solutionising heat treatment. The solution treatment is done in the single phase $\alpha$ region. Then the samples are usually quenched and then heat treated. The solutionising heat treatment not only makes the system homogeneous, but also gives the required supersaturation when the alloy is quenched to lower temperatures.

### 1.2.2 Aging in Al-Cu alloys

In Fig. 1 we show the hardness in certain Al-Cu alloys as a function of aging time at, say, 130°C. These alloys were initially solution treated in the single phase $\alpha$ region, quenched to room temperature and then aged at the given temperature. As is clear from these figures, the hardness increases with time at least in the initial stages of the aging treatment; however, in all alloys, the hardness starts dropping after some time; this drop in hardness with time is known as overaging. As shown in Fig. 2, broadly similar behaviour is also observed in Al-Cu alloys aged at 190°C. However, at this high temeprature,

the overaging sets in much earlier; further, the changes in hardness are more monotonous (with no pleateau regions).

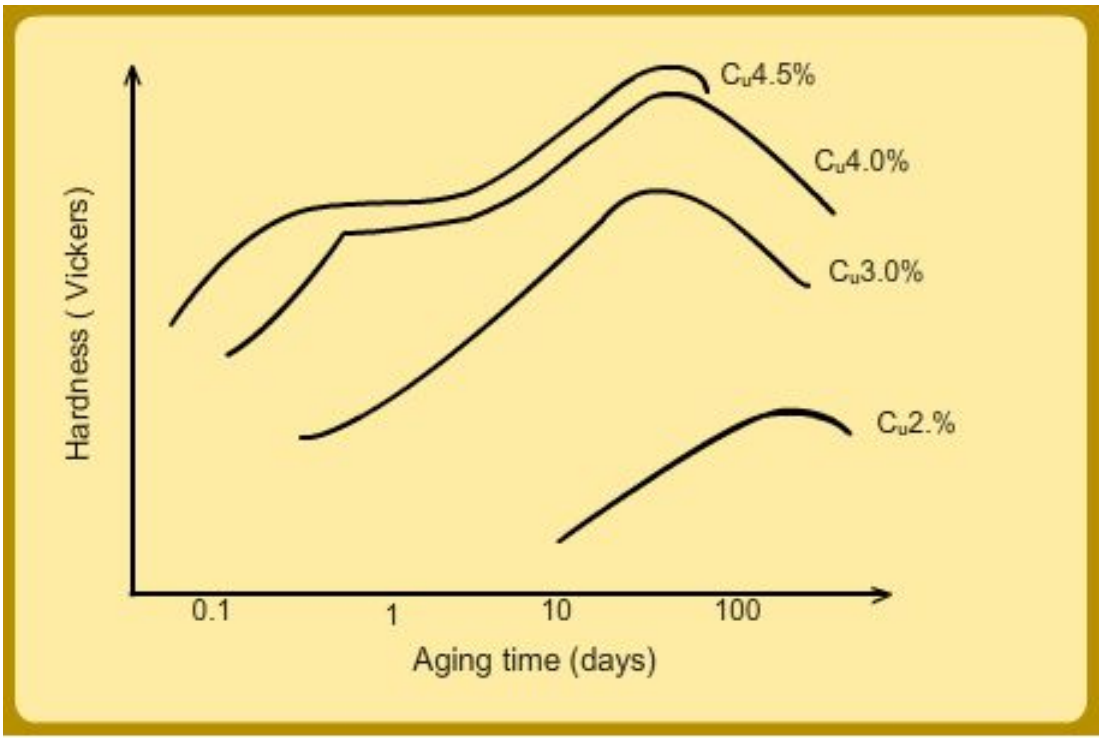


Figure 1: Aging curves at 130° C for Al-Cu system.

In Fig. 3 and Fig. 4, we show the aging curves; however, this time, we also superimpose the different phases that precipitate out of the matrix at these temperatures for the given times on the aging curves. There is a clear correlation

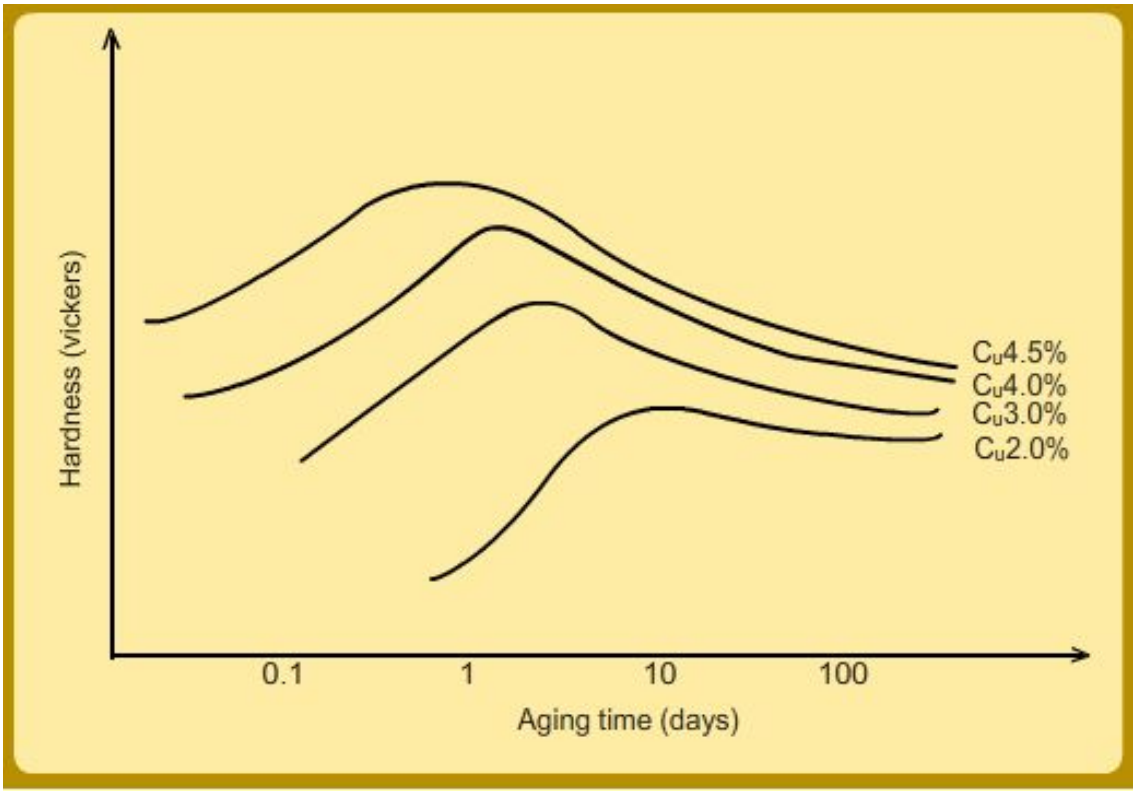


Figure 2: Aging curves at 190° C for Al-Cu system.

between the phases that form and the change in hardness; typical increases in hardness are associated with the formation of GP (Guinier-Preston) zones and $\theta''$ precipitates; in most cases, the formation of $\theta'$ leads to a decrease in hardness.

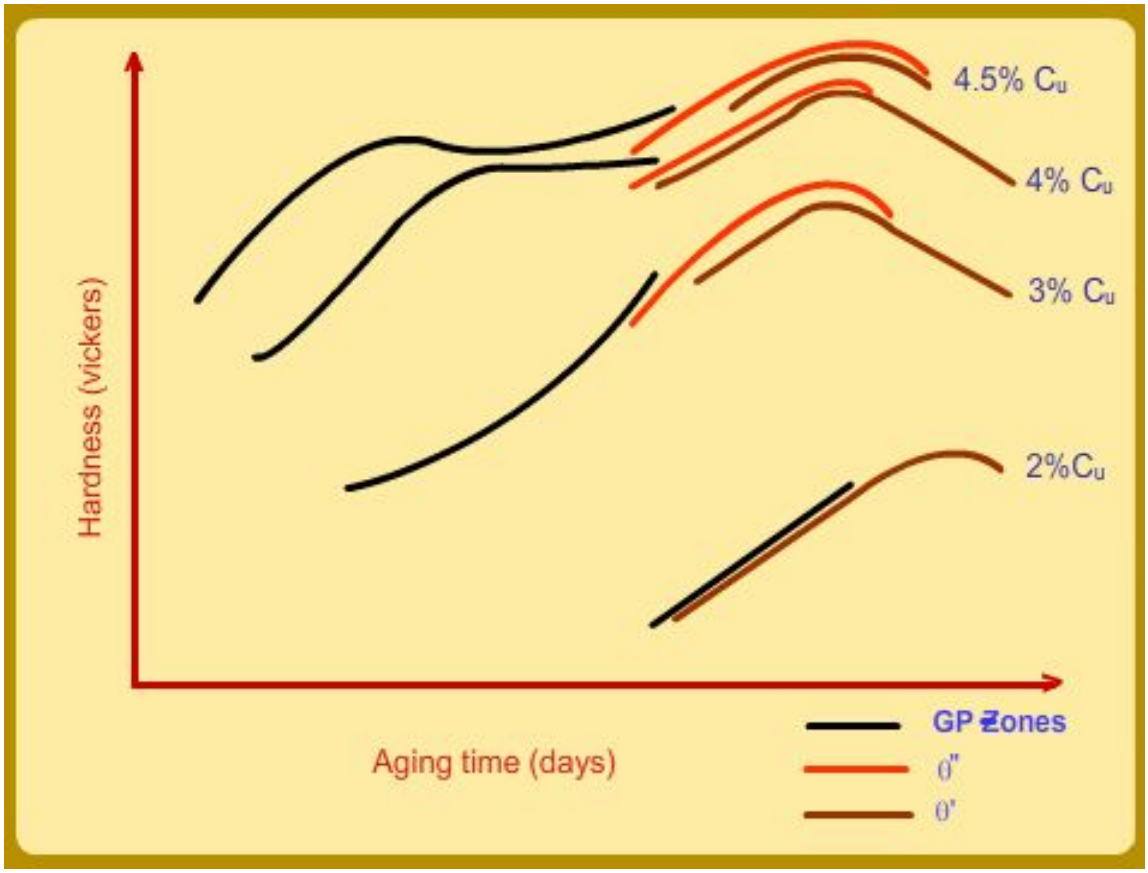


Figure 3: Aging curves with phases: 130°

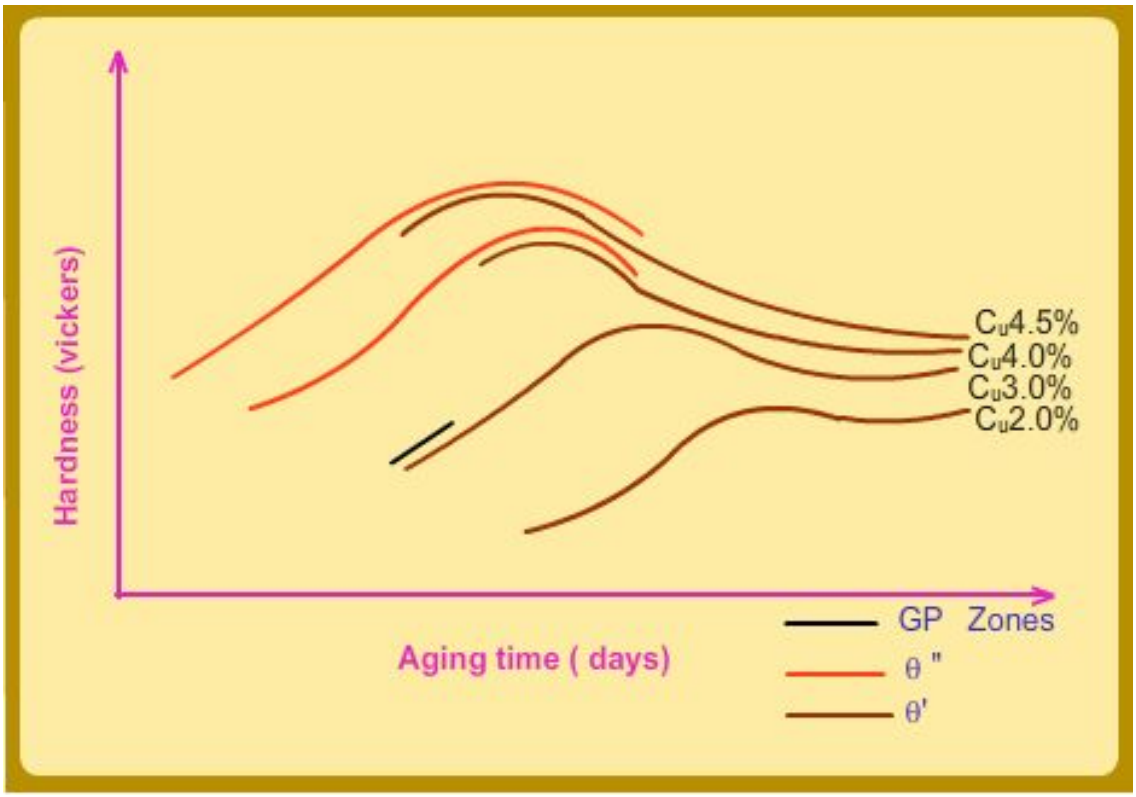


Figure 4: Aging curves with phases: 190°

Immediately after quenching to room temperature the only contribution to strengthening (that is, resistance to the movement of dislocations) comes from the solid solution: copper atoms at the aluminium sites which resist the movement of dislocations. However, as the GP zones form, the elastic stresses associated with the coherent GP zones resists the movement of dislocations contributing to hardness.

As the aging time increases, the coherent $\theta''$ phases that form, due to the misfit strains that they produce, manage to resist the movement of dislocations and hence lead to further hardening.

Finally the formation of semicoherent $\theta'$ can also increase the strength; however, in the case of both $\theta''$ and $\theta'$ if the particles are coarser or the volume fractions of these phases are smaller (and hence are further apart) it leads to a decrease in hardness since the dislocations can bow between the preciptiates and hence move in the matrix contributing the plastic deformation.

We also notice that at the higher temperature the peak hardness (the highest hardness that is achieved before overaging) is lower; this is because the lower driving force at the higher temperature for the formation of the $\theta''$ phase leads to a coarsely dispersed phase with lower volume fractions.

In the following sections, we discuss in detail the thermodynamics and kinetics of precipitation in age-hardenable Al-Cu alloys.

### 1.2.3 Phase diagrams and TTT diagrams

In Fig. 5, we show the Al-rich portion of the Al-Cu phase diagram (schematically). From the phase diagram, it is clear that the Al with a few percent copper is cooled from high temperature leads to the formation of a microstructure in which the $\theta$ phase precipitates out of the supersaturated $\alpha$ matrix. However, if an alloy of composition Al - 4 wt.%Cu is solutionised at say, 540°C, and the resultant $\alpha$ phase is rapidly quenched to room temperature, the solid solution is largely retained; if this alloy is kept at room temperature (or at any temperature below 180°C), a metastable phase known as Guinier-Preston zones (GP zones) is formed. Similarly, the aging treatment at other temperatures can produce other precipitates such as $\theta''$ and $\theta'$. The solvus for these metastable phases in shown in Fig. 6. Further, in Fig. 6, we also show the corresponding time-temperature-transformation curves for these metastable phase as well as the stable phase. In the following sections,

we describe the crystallography and interface structure of all these phases as well as the reasons for their formation.

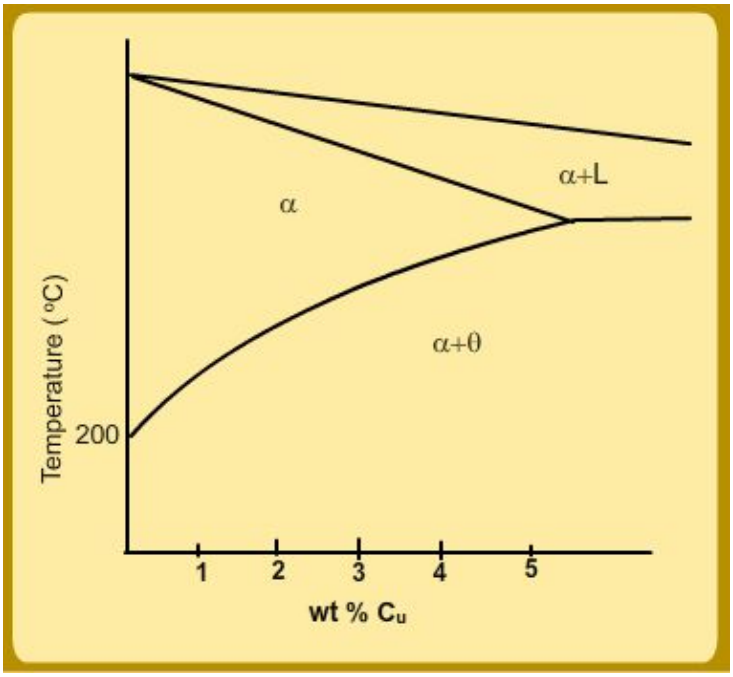


Figure 5: Al-rich portion of Al-Cu phase diagram.

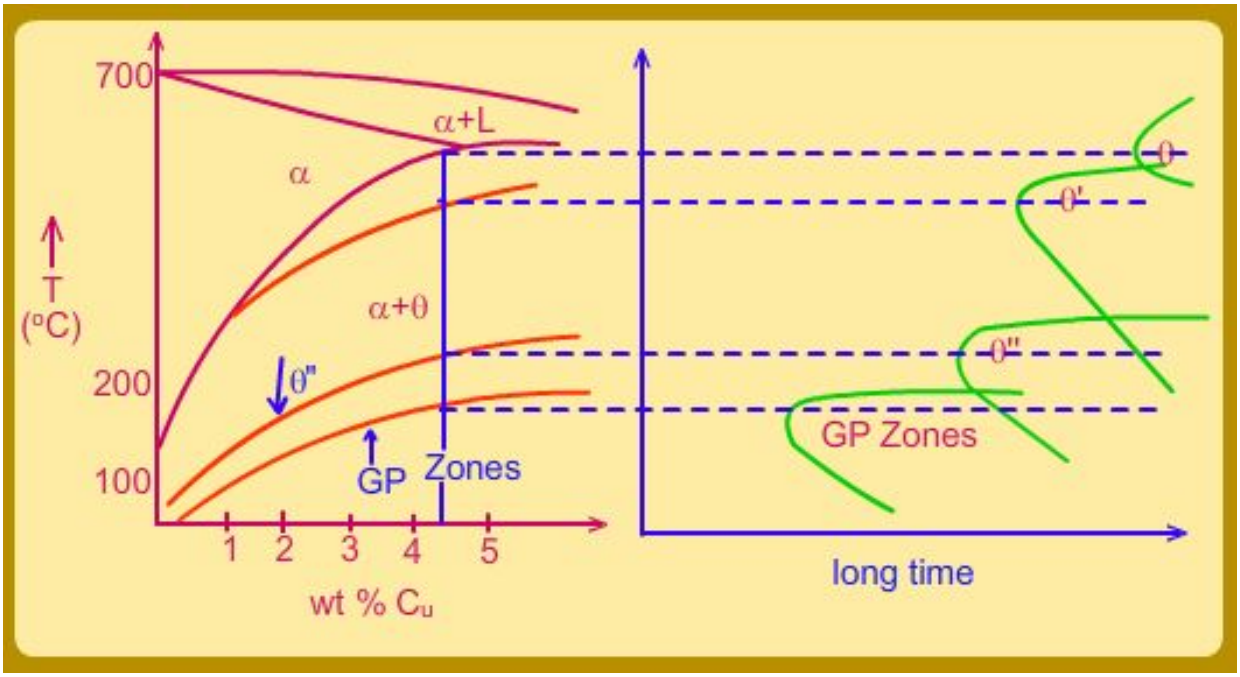


Figure 6: Metastable phases along with their TTT diagrams for Al-rich Al-Cu alloys.

### 1.2.4 GP zones and transition phases

The GP zones are copper rich; they are fully coherent with the matrix and hence very low interfacial energy. They are disk shaped and the disks are aligned along the elastically soft directions of the fcc matrix (¡100¿ in this case) in order to reduce the elastic energy associated with the coherency. The GP zones are (typically) about 10 nm in diameter, 2 atomic layers thick and are typically separated by about 10 nm.

The $\theta''$ is tetragonal; it is a distorted fcc structure with alternating copper and almuminium atoms on the (001) planes. It has a small misfit along the $c$ direction which is accomodated by elastic strain, and hence, it is also coherent with the matrix (with a habit plane of (001): that is $(001)_{\theta''}$ is parallel to $(001)_{\alpha}$). Because of the habit plane, the precipitates are generally platelike. Typical $\theta''$ precipitates are 100 nm in diamter and 10 nm in thickness.

The $\theta'$ is also tetragonal with an approximate composition of $CuAl_2$. They have the same orientation relationship as $\theta''$. The misfit in the other two directions are large and hence the interface is either semi-coherent (with misfit dislocations) and incoherent. The plane face (namely, (001)) is coherent though as size increases, it starts to lose coherency. The typical $\theta'$ precipitate is about 1 $\mu$m in diameter.

Finally, the equilibrium phase, $\theta$ is a complex body-centered tetragonal phase with approximate composition of $CuAl_2$ with incoherent interfaces.

The sequence of phases formed in Al-Cu alloys is as follows: $\alpha_0 \rightarrow \alpha_1 +$ GP zones $\rightarrow \alpha_2 + \theta'' \rightarrow \alpha_3 + \theta' \rightarrow \alpha_4 + \theta$ The schematic free energy versus composition curve in Fig. 7 shows the driving force associated with each step; as can be seen from the free energy versus composition diagram, the decrease in free energy with the formation of the metastable phase, say, GP zones for example, is lower compared to that of the precipitation of the equilibrium $\theta$ phase. However, the energy barrier for the nucleation of these metastable phases is lower; this is due to the coherency/semi-coherency of the interfaces which leads to lower interfacial energies in general. This difference in activation energy is shown schematically in Fig. 8.

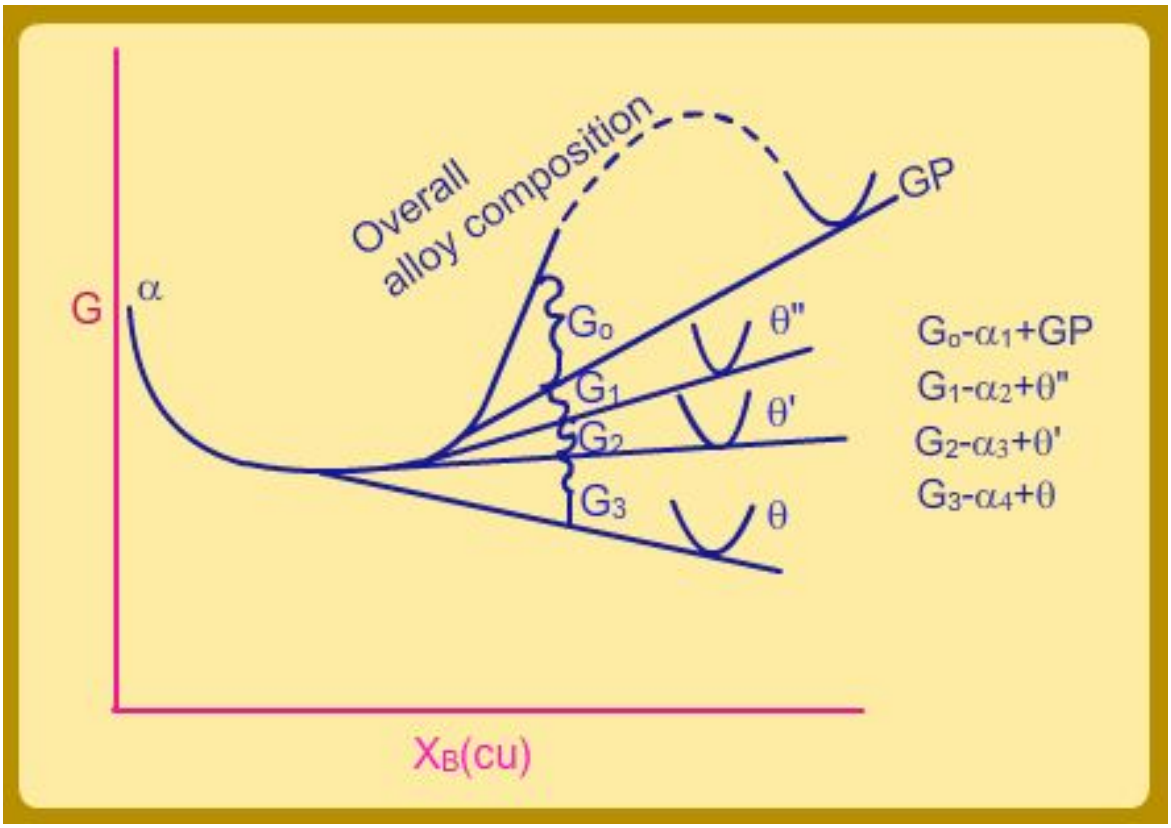


Figure 7: Driving forces for the formation of the metastable phases.

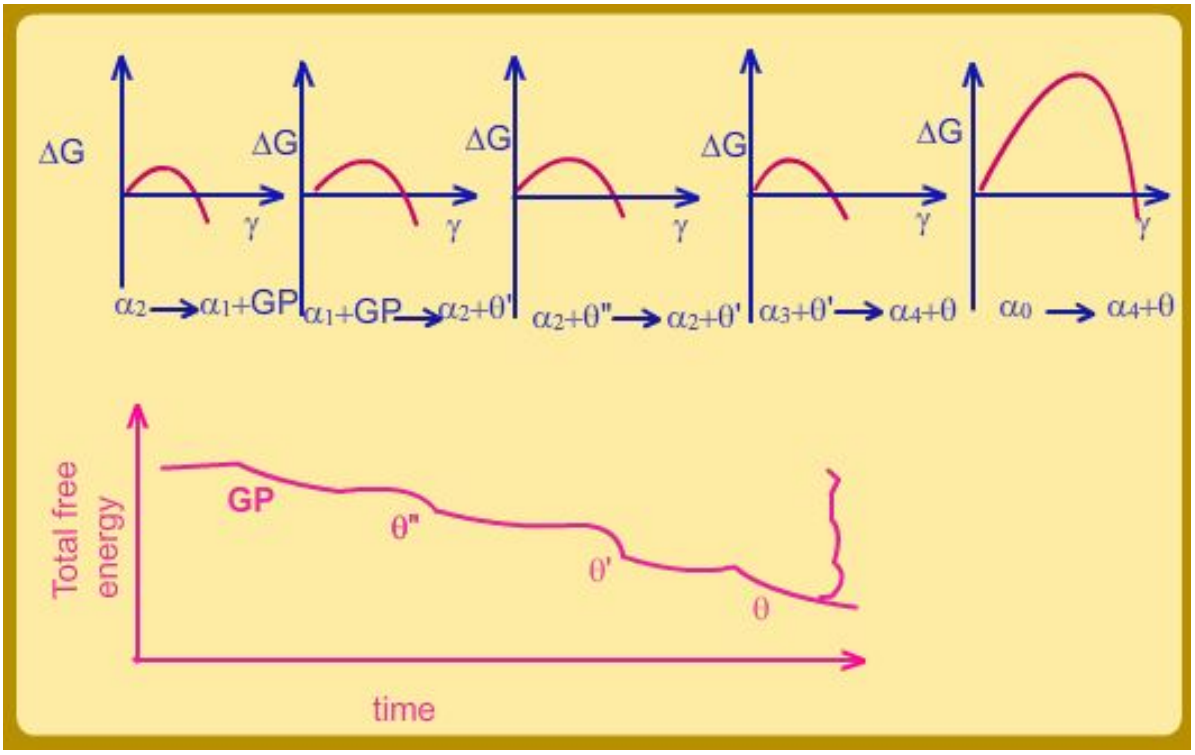


Figure 8: Differences in activation energies for the formation of metastable phases and the stable phase.

From the free energy versus composition diagram, it is also clear that the metastable phases, when co-exist, the more stable phase (the phase with lower free energy) will grow at the cost of the less stable phase due to the differences in composition of the $\alpha$ phase with which they are in contact; this is schematically shown in Fig. 9.

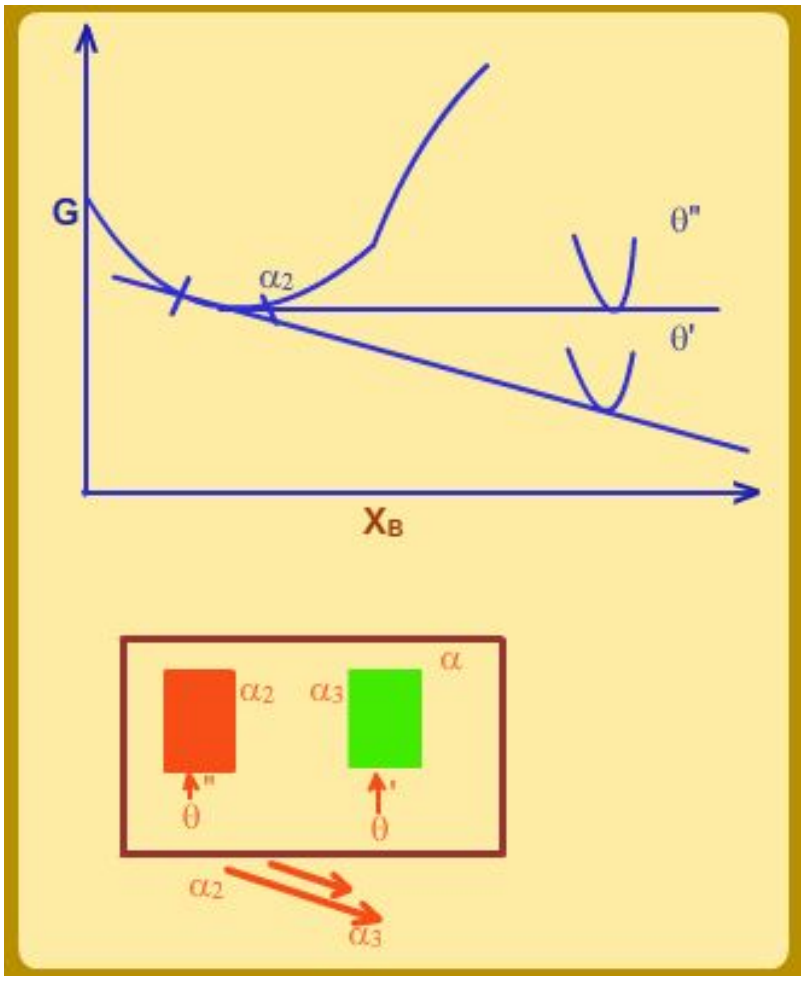


Figure 9: Growth of more stable phase from the less stable phase: the mechanism of the kinetics.

Finally, while GP zones are seem to be homogeneously nucleated (or heterogeneously, on excess vacancies), $\theta''$ nuclei are formed by the transformation of these GP zones; $\theta'$ typically nucleates on dislocations while $\theta$ nucleates either on grain boundaries or at the $\theta'$-matrix interface.

## 1.3 Precipitation hardening

The age hardenability of Al-Cu alloys is but one example of precipitation hardened alloys. There are many technologically important alloys that precipitation harden: Al based alloys (Al-Ag, Al-Cu-Mg, Al-Zn-Mg, Al-Mg-Si) and others (such as Cu-Be, Cu-Co,Fe-C, Fe-N, Ni-Cr-Ti-Al); in many of these alloys both the formation of GP zones and other similar microstructural features are seen.

## 1.4 Precipitate free zones

The equilibrium vacancy concentration increases exponentially with temperature (see tutorial below). Thus, when an alloy is quenched from the solutionising temperature, if the quenching is fast enough, there will be excess vacancies in in the alloy. Such vacancies, given enough time, will anneal out. Such annealing takes place via the formation of clusters of vacancies, absorption at dislocations and grain boundaries. In addition to the clustering of vacancies promoting heterogeneous nucleation by acting as nucleation sites, the presence of excess vacancies can also cause an increase in the diffusion rates and hence lead to faster growth of precipitates and GP zones. That the presence of excess vacancies affect diffusion can be shown experimentally by quenching the same alloy from two different temperatures to the same temperature and holding it at that temperature for the same amount of time; in such cases, the alloys quenched from the higher temperature have higher rate of formation of GP zones. Similarly lower rates of cooling or interruptions at an intermediate temperature that allows for vacancy concentration equilibration leads to reduced rates of transformation.

The excess vacancies can also lead to an interesting microstructural feature called precipitate free zones (PFZ). PFZs are zones with no precipitates in a system in the vicinity of grain boundaries, dislocations and inclusions. The formation of PFZ next to a grain boundary for example, can be explained

as follows: the excess vacancies in the alloy, in regions closer to the grain boundary, can anneal out fast because grain boundary can act as a sink for vacancies. This in turn affects the nucleation and growth of the precipitates in this region. As shown in Fig. 10, in the vicinity of the grain boundary, the vacancy concentration reaches to equilibrium pertaining to the aging temperature while away from the boundary in the bulk, the vacancy concentration corresponds to that of the solutionising temperature. This is turn is also conclusively shown by the change in the width of the PFA depending on the rate of quench: fast (slow) quenches lead to narrower (wider) PFZs. This is because the diffusion distances are affected by the time available for diffusion.

PFZs can also form by another mechanism associated with the nucleation of precipitates at the grain boundary; see the tutorial.

## 1.5 Elastic stress effects

In many alloys where precipitation takes place, the elastic stress effect can be very important. An exception to this is the Cu-Co alloys (Cu with 1-3% Co). In this system the elastic stresses are very small. Hence, these alloys are used as model systems for experimetnal validation of theories of homogeneous precipitation; see for example [3].

Elastic stress effects, when present, can lead to interesting microstructural features. The classic example for the elastic stress effects that manifest during precipitation are the formation of $Ni_3Al$ ($\gamma'$) precipitates of $L1_2$ structure (ordered fcc) from the Ni-rich ($\gamma$) fcc phase. For example, consider Ni-Al-Mo alloys of composition 5-12% Al and 2-13% Mo (See [4]). In these alloys, the Mo, when present, prefers to stay in the nickel rich matrix. However, the partial molar volume of Mo atoms are larger than Ni. Hence, they tend to increase the lattice parameter of the $\gamma$ phase. Hence, the misfit, defined as $\delta = (a_\gamma - a_{\gamma'})/a_\gamma$ changes from negative to positive through zero. The misfit has two important effects on the microstructure. First is what is known as the symmetry breaking transition: at small sizes, the precipitates are spherical; however, as the size increases, precipitates become more cube-like (as the $|\delta|$ increases, and, remain spherical when $\delta \approx 0$). Further, the precipitates also align along the $< 100 >$ directions of the $\gamma$ matrix (which is the elastically

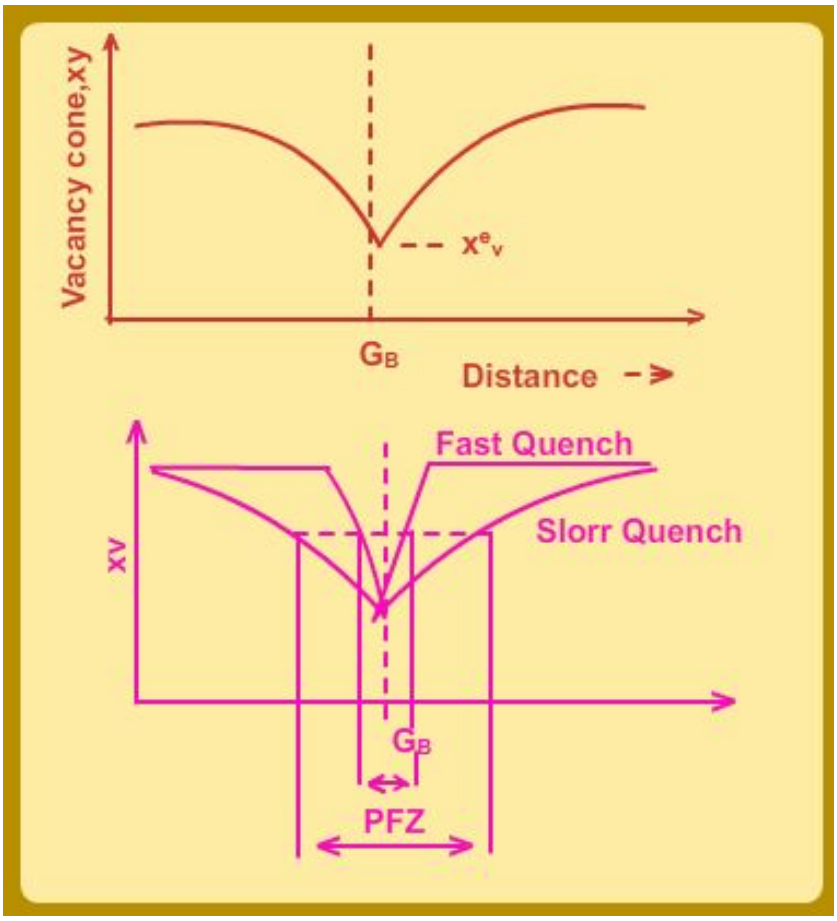


Figure 10: Vacancy concentration at the GBs and their vicinities as a function of quenching rate.

soft direction). See Fig. 11 for the schematic microstructures and the tutorial for the calculation of the critical size at which symmetry breaking transition will take place).

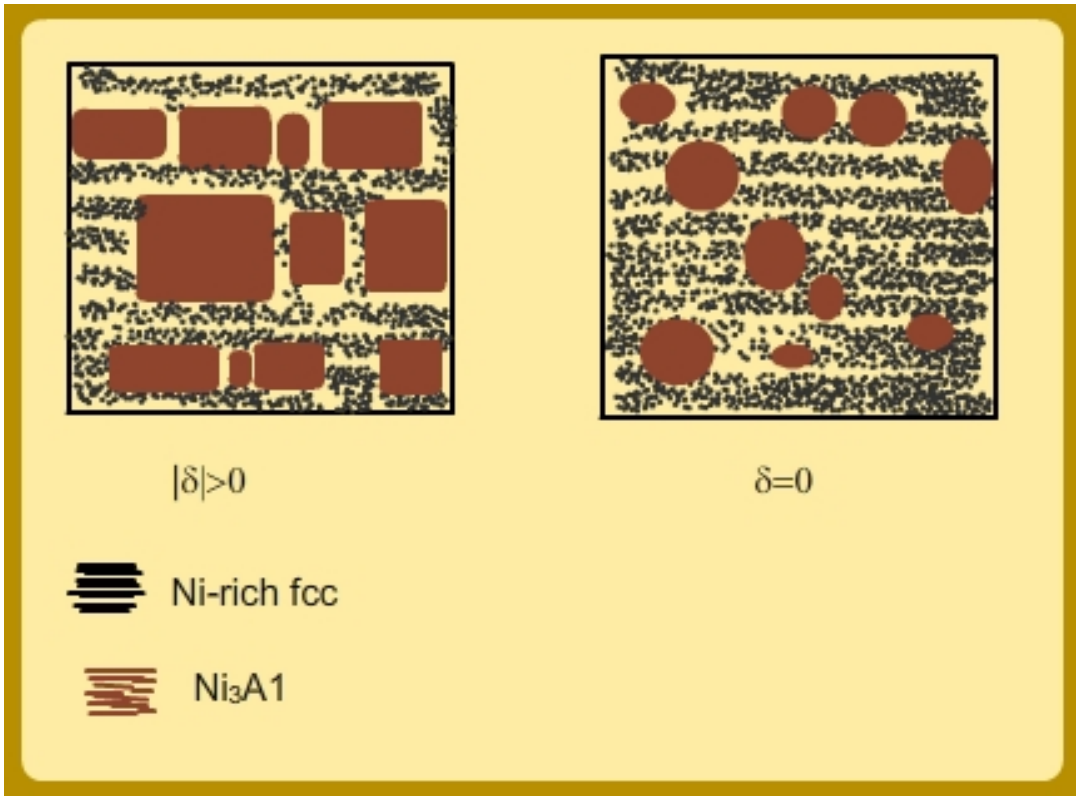


Figure 11: Effect of misfit on microstructure in Ni-Al-Mo alloys.

## 1.6 Fe-C alloys

Consider the phase diagram of Fe-C shown in Fig. 12 and the following heat treatment of the Fe-0.15 wt.% C steel; the alloy is initially allowed to partially transform to ferrite at various temperatures below $A_3$ and is quenched in water. The microstructures that result from these heat treatment processes are shown schematically in Fig. 13.

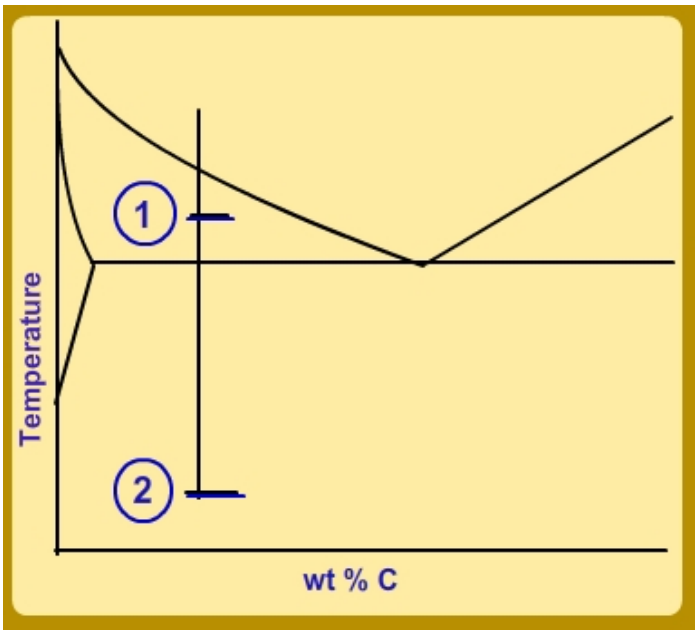


Figure 12: Phase diagram of the Fe-C system at low carbon compositions.

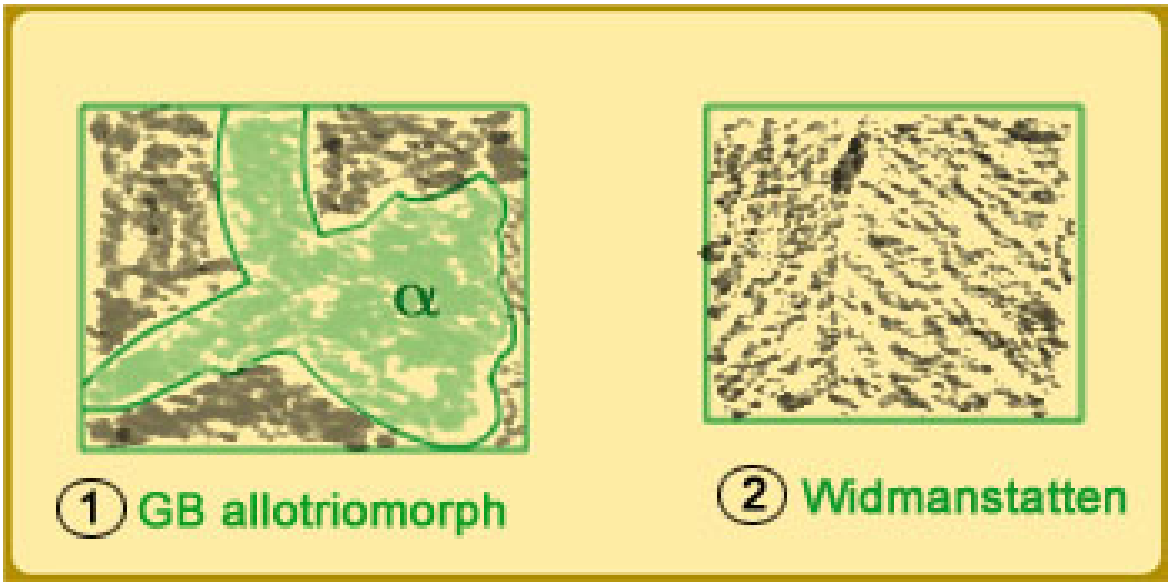


Figure 13: Morphologies at different undercoolings.

The microstructures consist of ferrite ($\alpha$) and martensite which is formed from the untransformed austenite ($\gamma$) during the quench.

At small undercooling below $A_3$, the ferrite nucleates on austenite grain boundaries; further it grows in a blocky manner as shown leading to a microstructural feature known as grain boundary allotriomorph. The allotriomorphs consist of both smoothly curved (and hence, incoherent) and facetted (and hence, probably semi-coherent) interfaces.

On the other hand, at larger undercoolings, even though the nucleation is still at the grain boundaries, the ferrites grow from the boundaries as plates leading to a microstructural feature called Widmanstatten side plates; the larger the undercooling, the finer the plates.

### 1.6.1 Grain boundary nucleation and allotriomorph morphology

Consider the nucleation of the ferrite at the austenite grain boundaries. The two grains on either side of the boundary have different orientation. When the precipitate nucleates at the grain boundary, it can either have incoherent interfaces with both the grains or semi-coherent/coherent interface with one or both the grains. It is very rare to find a grain boundary precipitate to have semi-coherent / coherent interface with both the grains. Since having a semi-coherent / coherent interface would lead to a lower interfacial energy (and hence smaller barrier for nucleation), the system prefers such a nuclei over the case where the boundaries with both the grains are incoherent: see Fig. 14. During growth of these nuclei, the semi-coherent / coherent interfaces (which are facetted), in general tend to grow slower than the incoherent interfaces (which are curved). Thus, one finds that allotriomorphs to have both curved and facetted interfaces.

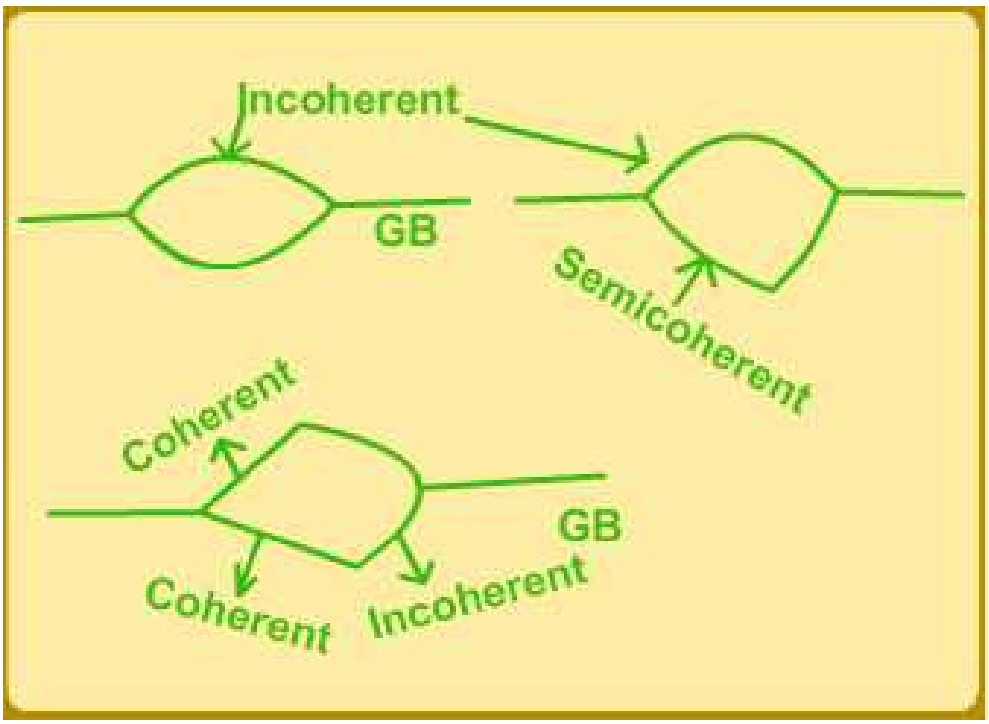


Figure 14: Nucleation at the grain boundary: types of interfaces.

### 1.6.2 Orientation relationships of Widmanstatten sideplates

Windmanstatten sideplates are an example of a bcc precipitate in an fcc matrix. The orientation relationship in such systems lead to semi-coherent interfaces that are quite complex in structure. Typically, the closest packed planes in both the phases are almost parallel to each other; there are two specific orientation relationships that are known to exist in such systems. They are are follows:

**Nishiyama-Wasserman (N-W)**

$(110)_{\text{bcc}}$ // $(111)_{\text{fcc}}$
$[001]_{\text{bcc}}$ // $(\bar{1}01)_{\text{fcc}}$

**Kurdjumov-Sachs (K-S)**

$(110)_{\text{bcc}}$ // $(111)_{\text{fcc}}$
$[1\bar{1}1]_{\text{bcc}}$ // $(0\bar{1}1)_{\text{fcc}}$

## 1.7 Tutorial problems and questions

1. Derive an expression for the change of vacancy concentration with temperature.

2. Consider the formation of GP zones in an Al-Cu alloy aged at room temperature; if GP zones with interzone distance of about 50 nm spacing are found after about a day, estimate the intediffusivity.

3. Explain how PFZ can form due to nucleation at grain boundaries.

4. Consider a Ni-base superalloy; the interphase interfacial energy between the matrix and the precipitate phase is 100 $\text{mJ/m}^2$. The misfit is 0.1% and the shear modulus 80 GPa. Calculate the size at which the elastic stress effects will become dominant.

## 1.8 Solutions to the tutorial

1. Consider a pure material. Let us consider the case wherein some of the lattice sites are left vacant. Production of such sites costs energy because one needs to break atomic bonds to remove an atom from its lattice position. Hence, formation of vacancies always increase the enthalpy. However, introduction of vacancies also increases the configurational entropy. Hence, at any temperature, the optimum vacancy concentration is obtained by minimizing the corresponding free energy.

   For simplicity's sake, let us assume that the change in enthalpy $\Delta H = X_v \Delta H_v$ where $X_v$ is the vacancy concentration and $\Delta H_v$ is the enthalpy of formation per mole of vacancies; that is, each vacancy increases the enthalpy of the system by $\Delta H_v / N_{Avo}$ where $N_{Avo}$ is the Avogadro number.

   There are two contributions to the entropy due to the formation of vacancies: the first is the change in thermal entropy which follows due to the changes in vibrational frequencies of atoms in the vicinity of vacant sites; this contribution ($\Delta S_v$ per mole of vacancies) is small. The second is the configurational entropy which can be obtained using random dispersion of vacancies on lattice sites. Hence

   $$\Delta S = X_v \Delta S_v - R[X_v \ln X_v + (1 - X_v) \ln (1 - X_v)] \qquad (1)$$

   at the change in enthalpy $\Delta H = X_v \Delta H_v$ where $X_v$ is the vacancy concentration and $\Delta H_v$ is the enthalpy of formation per mole of vacancies; that is, each vacancy increases the enthalpy of the system by $\Delta H_v / N_{Avo}$ where $N_{Avo}$ is the Avogadro number.

   There are two contributions to the entropy due to the formation of vacancies: the first is the change in thermal entropy which follows due to the changes in vibrational frequencies of atoms in the vicinity of vacant sites; this contribution ($\Delta S_v$ per mole of vacancies) is small. The second is the configurational entropy which can be obtained using random dispersion of vacancies on lattice sites.

   Thus, the total (molar) free energy of a system containing $X_v$ mole of vacancies is given by

   $$G = G_A + \Delta H_v X_v - T \Delta S_v X_v + RT[X_v \ln X_v + (1 - X_v) \ln (1 - X_v)] \quad (2)$$

where $G_A$ is the molar free energy for the material without vacancies. In Fig. 15, we show these energies (and the equilibrium vacancy concentration).

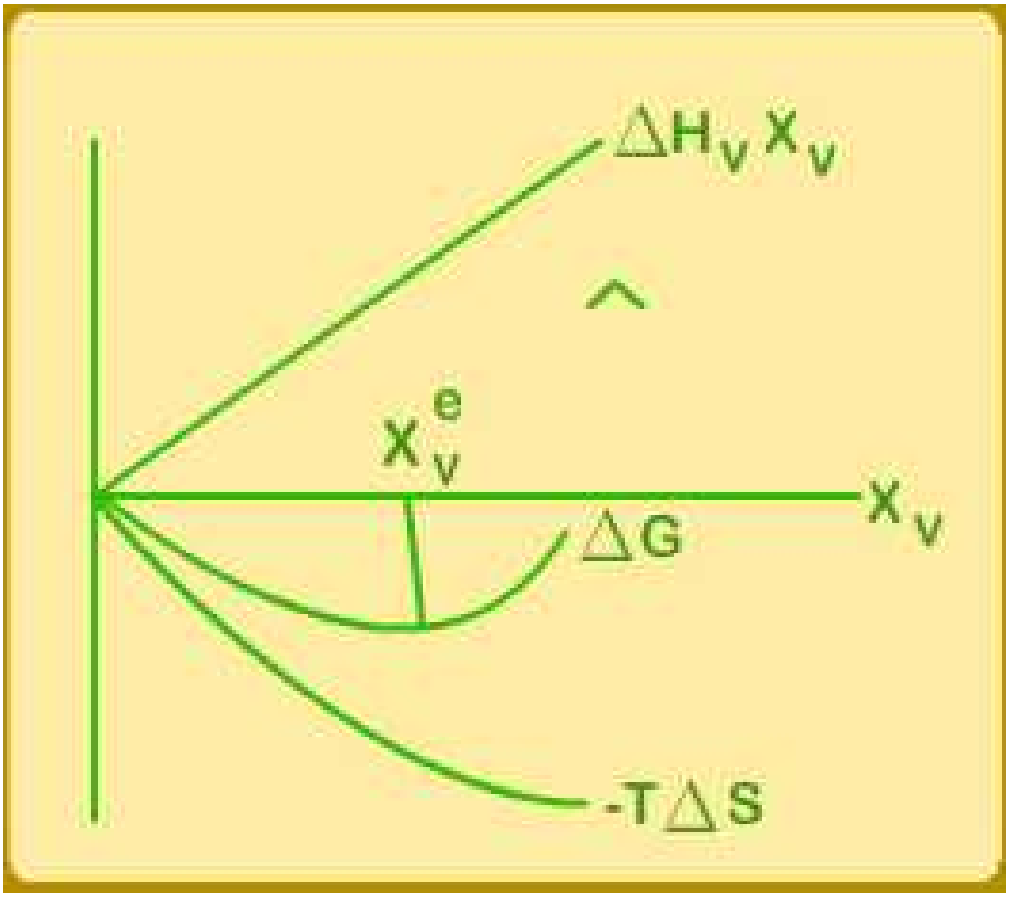


Figure 15: Equilibrium vacancy concentration.

The equilibrium vacancy concentration is then obtained by maximizing the free energy with respect to $X_v$; that is, by solving the following

equation:

$$\left(\frac{dG}{dX_v}\right)_{X_v=X_v^e} = 0 \tag{3}$$

Thus,

$$\Delta H_v - T\Delta S_v + RT \ln X_v^e = 0 \tag{4}$$

where we have further assumed that $X_v << 1$.

In other words,

$$X_v^e = \exp\left(-\frac{\Delta G_v}{RT}\right) \tag{5}$$

That is, with temperature, the vacancy concentration increases exponentially.

2. $D = \lambda^2/4t$ where $D$ is the diffusivity and $\lambda$ is the interzone distance. Hence, for the given data, the estimate of diffusivity is $\approx 1.4 \times 10^{-21}$ $m^2$/sec. Note that this diffusivity is very high for the temperature considered. Hence, this effective fast diffusion must be a result of availability of excess quenched in vacancies.

3. In Fig. 16 we show schematically the formation of grain boundary precipitates. These precipitates will suck in solute from the surrounding matrix. As shown schematically in the figure, this will lead to PFZs on either side of the boundary.

4. The interfacial energy is a per unit area quantity while the elastic energy is a per unit area quantity. Hence, as the size of the precipitate increases, the elastic energy becomes dominant. One approximate calculation of the size at which elastic energy dominates is obtained by dividing the interfacial energy by the elastic energy. Thus, we obtain a characteristic size of about 1 micron or so.

## 1.9 Supplementary information

The story of the discovery of age hardening in duralumin is an interesting one; it is recounted by Polmear (Aluminium alloys–a century of age hardening, Materials forum, Volume 28, 2004) and Hornbogen (Hundred years of

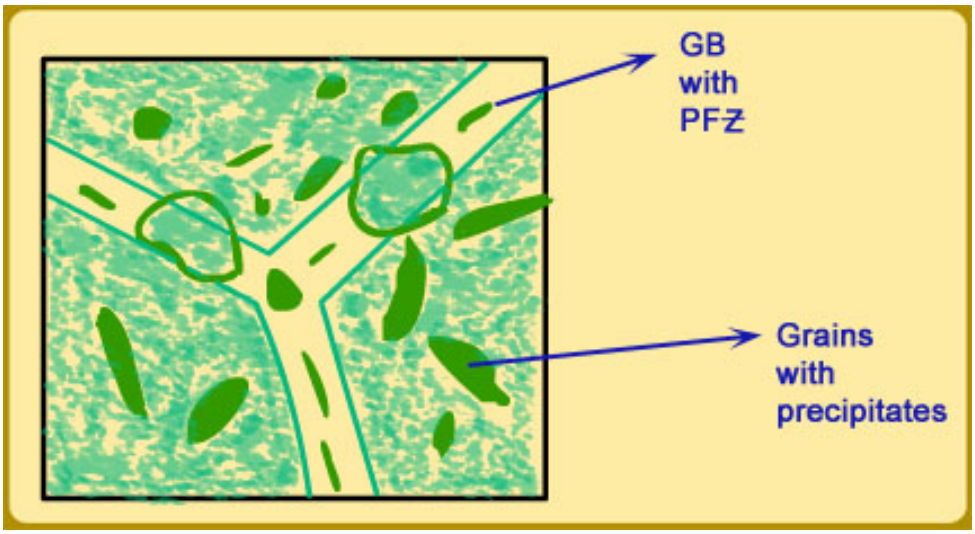


Figure 16: PFZ formation due to grain boundary precipitation.

precipitation hardening, Journal of light metals, Volume 1, 2001). According to these two accounts, Alfred Wilm, a German scientist, was experimenting with Al-Cu alloys containing small amounts (less than 1%) of Mn and Mg. Sometime in 1906, on a Saturday morning, just before noon, he heated the alloy to 520$^o$C and quenched. He and his assistant Jablonski had enough time only to make a quick hardness measurement. After that, Wilm went for sailing in river Havel. The following Monday, when Jablonski and Wilm measured the hardness, they found it to be much higher compared to their previous measurement. Initially, Wilm and Jablonski suspected that their hardness measurements are wrong. However, after repeated experiments and calibration of hardness measurements they conclusively proved that the process of after heating the given Al-Cu alloy to 520$^o$C, then quenching it to room temperature, and keeping it at room temperature for a few days, resulted in increased hardness; see the schematic in Fig. 17 for what came to be known as "age hardening" process and is probably the most important metallurgical discovery of the last century.

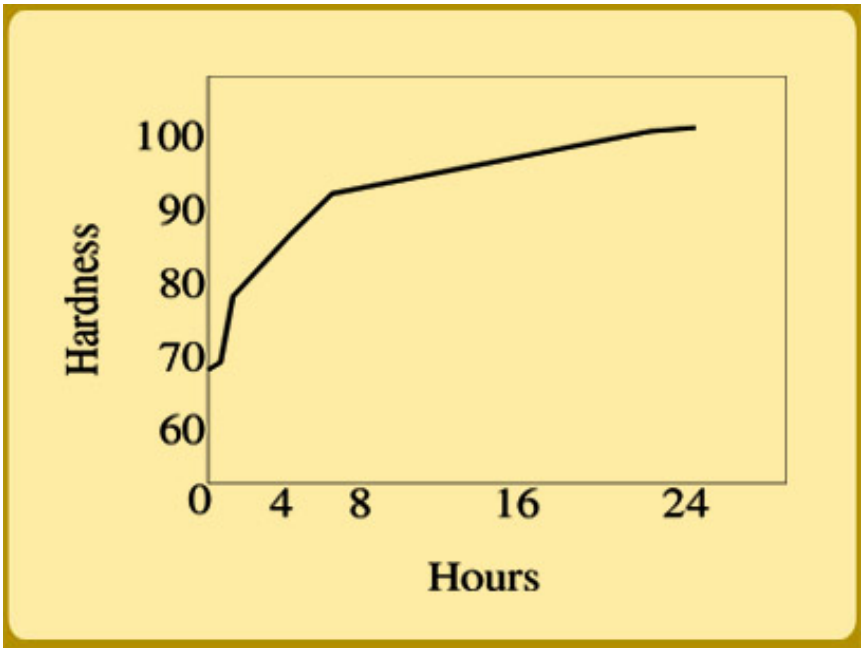


Figure 17: Schematic of age hardening reported by Alfred Wilm (in an alloy of Al-Cu that was named as duralumin later).